RICE UNIVERSITY

422 **nm Laser**

by

Clayton Earl Simien

A Thesis Submitted
in Partial Fulfillment of the
Requirements for the Degree

Masters of Science

Approved, Thesis Committee:

Thomas C. Killian, Chairman
Assistant Professor of Physics and
Astronomy

Randall G. Hulet
Fayez Sarofim Professor of Physics and
Astronomy

Paul A. Cloutier
Professor of Physics and Astronomy

Houston, Texas

September, 2004

ABSTRACT

422 **nm Laser**

by

Clayton Earl Simien

A 422 nm laser was constructed for the purpose of studying a strontium ultracold neutral plasma. Since strontium ions have atomic lines in the visible, we can optically image the plasma via the $^{88}Sr^{+}$ $2S_{1/2} \rightarrow 2P_{1/2}$ transition using 422 nm light. We produce light at this wavelength by converting infrared light at 844 nm from a commercial semiconductor infrared diode laser via second-harmonic generation in an semi-monolithic linear enhancement cavity. This thesis will cover the experimental details pertaining to nonlinear optics, optical resonator design, and locking electronics used to create a 422 nm laser.

Acknowledgments

First, I would like to acknowledge my Lord in Heaven and His Son, my Savior, Jesus Christ for Their grace and mercy in blessing me with family, friends, and mentors whose help has made it possible for me to complete my master's project. Particular, Dr. Thomas Killian, for carrying me through this project on his shoulders of patience and expertise. Ying-Cheng Chen for his invaluable assistance. My friend, my brother, Musie Gherbermicheal for his wisdom, encouragement, and friendship which has been food for my soul. Finally, I would like to give a special thanks to my family, for all their love, support, sacrifice, and struggle that has allowed me to survive, give me purpose, and achieve this level in my education.

Contents

List of Figures

Chapter 1
Introduction

The motivation for this thesis is to construct a laser to optically study a strontium ultracold neutral plasma. Using strontium is vital to the experiment because strontium ions, $^{88}Sr^{+}$, have an allowed transition in the visible at 421.7 nm. This transition makes it possible to probe the plasma via fluorescence or absorption imaging. This has never been done before and opens many experimental possibilities.

The purpose of this thesis is to describe the blue laser source for optical imaging. There are no commercial lasers available at this wavelength. So, we must use the nonlinear optical technique of second harmonic generation to frequency double an existing infrared commercial laser to produce a blue laser source. First, we shall briefly review ultracold neutral plasmas, previous diagnostic schemes, and the advantages of optically probing the ultracold plasma.

1.1 Ultracold Neutral Plasmas

Study of ultracold neutral plasmas started at the National Institute of Standards and Technology (NIST) in Gaithersburg, Maryland in 1999 [5]. These experiments begin with laser cooled and trapped metastable xenon [1]. To produce the plasma, the cooled and trapped xenon atoms were photoionized barely above threshold using a narrow bandwidth laser. Due to the small electron-ion mass ratio, the electrons in the photoionized sample had initial kinetic energies approximately equal to the difference between the photon energy and the ionization potential. The initial kinetic energy for the ions was in the mK range, and the electron kinetic energy in the 1-1000K range. These energy ranges are remarkably different from most ionized gases found in the universe (Figure 1.1). Interest in these system stems from the question of whether plasmas behave differently in this regime.

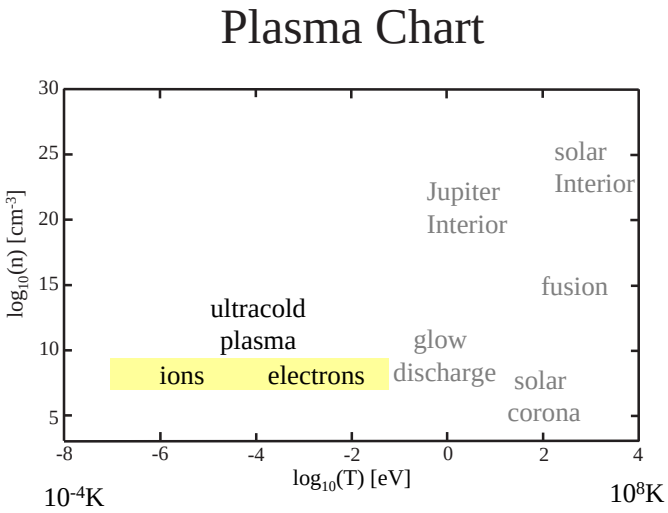

Figure 1.1 This is an illustration of various regimes of plasma in terms of temperature and density.

1.2 Previous Ultracold Plasma Diagnostics Schemes

Ultracold neutral plasmas have previously been studied by monitoring electrons as they escape from the plasma. An applied DC electric field directs the charges to a single-electron multiplier for detection. These signals reveal the dynamics of the plasma. Figure 1.2 illustrates an electron signal from an ultracold neutral plasma of strontium. The first peak represents electrons that leave the sample and create a small charge imbalance ($< 5\%$), thereby forming a Coulomb well that traps the remaining electrons. The second peak, which occurs on a longer timescale, indicates electrons that escape as the ultracold plasma expands, and the Coulomb well becomes shallower.

It is possible to perform experiments on the system during the expansion. For example, at NIST, radio-frequency induced plasma oscillations were used to map the plasma density distribution [6]. The plasma oscillation frequency is related to the

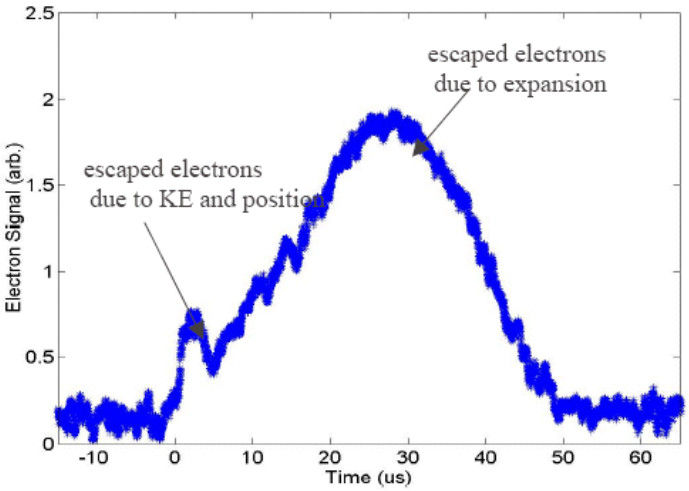

Figure 1.2 Electron signal from an ultracold strontium plasma created by photoionization at t=0. The first peak at about 1 μs represents electrons that leave the sample and create the charge imbalance and Coulomb potential well. The second peak represents electrons that leave the plasma as a result of expansion.

electron density according to the following expression,

$$f_e = (\frac{1}{2\pi})\sqrt{\frac{e^2 n_e}{\epsilon_o m_e}}, \tag{1.1}$$

where e is the electric charge, n_e is the electron density, and m_e is the electron mass. Figure 1.3a illustrates change in the electron signal of an ultracold xenon plasma when an rf field is applied. When the rf field is on resonance with the average electron gas density in the plasma, energy is pumped into the system. This produces the plasma oscillation response on the electron signal. The responses arrives later for lower frequency since the density of the plasma decreases in time (Fig. 1.3b).

1.3 Optically Imaging an Ultracold Plasma

Previous ultracold plasma diagnostic methods as described above are indirect and greatly limit the amount of physics one can learn. For instance, in the rf experiments performed at NIST, the diagnostics were only sensitive to the average density in the cloud.

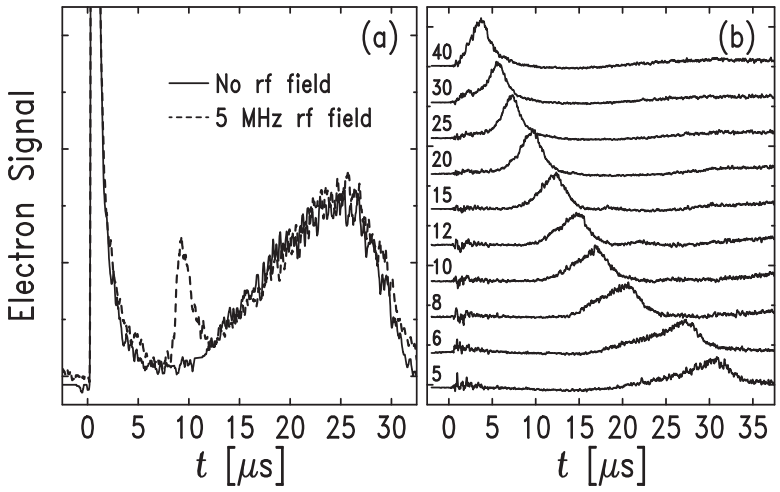

Figure 1.3 Electron signals from ultracold plasmas created by photoionization at t=0. (a) If an rf field is applied during the expansion, resonant excitation of plasma oscillations produces an extra peak on the electron signal. (b) For each trace, the rf frequency in MHz is indicated, and the nonresonant response has been subtracted. The resonant response arrives later for lower frequency, reflecting expansion of the plasma [6].

Optical imaging offers a better way to study the dynamics of the plasma. Probing the plasma through light scattering or absorption imaging would allow temporal, spatial, and spectral resolution of the ultracold neutral plasma. For example, the density profile can be imaged directly to monitor the plasma density as a function of time. To do this would be of great interest, since ion acoustic waves may be visible in the plasma density profiles, and measuring their group velocities may provide a diagnostic of the electron temperature, which is crucial for characterizing phenomena and comparing experiment with theory.

Imaging is also a first step toward laser cooling and trapping ultracold neutral plasmas. The ability to confine ultracold neutral plasmas in this manner will open up a new avenue of study in physics. Therefore enabling fundamental experiments on strong coupling [2], recombination [3], and ion-ion thermalization [4].

1.4 Outline

This thesis will describe the construction of a blue laser source at 421.7 nm. In chapter 2 we will discuss second-harmonic generation. Next, in chapter 3 we will go over the gaussian optics of resonators. In chapter 4 we will describe our optical resonator, discuss the experimental procedures to produce light at 421.7 nm, and analyze the performance of our blue laser source. Chapter 5 will cover the feedback electronics used to stabilize our laser system. Finally, in chapter 6, we will conclude this thesis with a brief discussion on the limitations of our blue laser source and display some preliminary imaging results.

Chapter 2
Second Harmonic Generation

This chapter discusses the concepts of Second-Harmonic Generation, and gives a brief description of the properties of potassium niobate.

2.1 Theory

Nonlinear optical phenomena in the interaction of light with a particular media is a result of the nonlinear nature of the polarization, which can be written in terms of the electric field E as:

$$P = \varepsilon_o \chi_1 E + \varepsilon_o \chi_2 E^2 + \varepsilon_o \chi_3 E^3, \tag{2.1}$$

where χ_1 is the linear susceptibility, χ_2 is the second-order susceptibility, and χ_3 is the third-order susceptibility. The term χ_2 is responsible for second- harmonic generation.

Second-harmonic generation is a nonlinear process in which an electromagnetic wave with frequency ω is converted into one at frequency 2ω. Consider an electromagnetic field with frequency ω_1=ω travelling along the z-axis through a crystal with a non-zero χ_2. This interaction of light with the material will create a polarization wave in the crystal with frequency ω_2=2ω. This polarization wave will then produce radiation at ω_2. The power of this radiation is related to the power at ω with beam area A by the following relation:

$$P_{\omega_2} = [\frac{2\eta_o^3 \omega_2^2 d_{eff}^2 L^2}{A}] P_{\omega_1}^2 (\frac{\sin \frac{\triangle kL}{2}}{\frac{\triangle kL}{2}})^2 = \xi_{nL} P_{\omega_1}^2 (\frac{\sin \frac{\triangle kL}{2}}{\frac{\triangle kL}{2}})^2, \tag{2.2}$$

where

$$\Delta k = \frac{2\omega_1 (n_1 - n_2)}{c}. \tag{2.3}$$

L is the length of the medium, d_{eff} is the nonlinear coefficient of the doubling crystal, and η_o =$377/n_1$ [7]. The term ξ_{nL} is the nonlinear- conversion efficiency. n_1 and n_2 are the index of refraction at ω_1 and ω_2 respectively.

2.2 Phase Matching

In Eq. 2.2 we can see that second-harmonic power is maximized when $\triangle$kL=0. When this happens, the second harmonic wave and fundamental wave inside of the material are phase matched. Physically this occurs when n_{ω_1}=n_{ω_2}, which means that both waves must have the same phase velocities inside the crystal. If the phase velocities of the two waves are not equivalent, then second harmonic waves generated at different planes throughout the crystal will destructively interfere with each other, as described by the sinc function in Eq. 2.2, thereby resulting in low ω_1 to ω_2 conversion efficiency.

Usually in materials, $n_{\omega_1} > n_{\omega_2}$, therefore phase matching is not achievable (dispersion effect). However, in birefringent materials, materials that posses different values of indicies of refraction in different directions, the phase matching condition n_{ω_1}=n_{ω_2} can be satisfied: light with frequency ω_1 is polarized along one axis of the crystal, while light with frequency ω_2 is generated along another perpendicular crystal axis.

2.3 Potassium Niobate

The frequency doubling crystal is required to be sufficiently birefringent to satisfy the phase matching criterion and optically transparent at both the fundamental and second harmonic wavelengths. It should also have a large non-zero d_{eff}. Potassium Niobate ($KNbO_3$) meets these requirements, and it is used in most system for frequency doubling into the blue-green spectral range. $KNbO_3$ is a biaxial crystal having principal (symmetric) axes with refractive indicies $n_a \neq n_b \neq n_c$ (a, b, and c are subscripts used by convention to denote the principal axis of the crystal).

In $KNbO_3$ phase matching can be achieved either by changing the angle at which the fundamental wave propagates with respect to the optical axis of the crystal, or by tuning the temperature of the crystal (Type I), since the index of refraction is

also temperature dependent. For our purpose, temperature-tuned phase matching is suitable, since $KNbO_3$ can be non-critically temperature-tuned phase matched for wavelengths from 840-1080 nm, which is a consequence of the strong temperature dependance of the refractive index along the c-axis. In Type I non-critical temperature-tuned phase matching the input and second harmonic beams are set-up to propagate along the a-axis of the crystal (a principal axis of the crystal), which has the advantage of a larger angular acceptance bandwidth and a vanishing walk-off angle [8]. The polarizations of the two beams are along the b-axis and c-axis respectively. The temperature of the crystal in this type of configuration is adjusted such that the refraction index experienced by the harmonic wave (polarized along c-axis) becomes the same as the refraction index experienced by the fundamental wave.

In addition, $KNbO_3$ is optically transparent from 400-3400 nm. It also has a d_{eff} approximately -21 pm/V. This value is a factor of four larger than most doubling crystals. For instance, $LiNbO_3$ d_{eff} is approximately 5.3 pm/V [9],[10].

Chapter 3
844nm Enhancement Optical Resonator

In this chapter the theoretical concepts used when designing an optical resonator will be discussed. This includes the motivation for the use of an optical resonator for second harmonic generation, gaussian modes and beams inside an optical resonator, and the coupling of light from an external source into an optical resonator.

3.1 Motivation

Equation 2.2 illustrates that the second harmonic power depends quadratically on the fundamental power. Thus, large amounts of fundamental power will result in high conversion efficiencies. Unfortunately, standard inexpensive continuous wave lasers do not produce powers that will yield significant conversion from infrared-to-blue. However, we can enhance the modest powers from commercial lasers with the use of an optical resonator.

An optical resonator is a set of two or more mirrors configured to allow light to propagate in a closed path. The enhancement of an optical resonator results from the effective number of round-trips the light makes along its closed path. For an optical resonator consisting of two mirrors having reflectivities R_a and R_b, the circulating power inside the optical resonator is expressed as [14]:

$$P_c = \frac{(1 - R_a)P_{input}}{[1 - \sqrt{R_a R_b(1 - \ell - C)}]^2} = bP_{input}, \tag{3.1}$$

where P_{input} is the input power of the laser, ℓ is the resonator round-trip parasitic loss excluding the input mirror transmission T_a and conversion to blue, and b is the effective number of photon round-trips in the cavity. The term C=$\xi_{nL}P_c$ is infrared-to-blue conversion loss (IBCL), which describes the fraction of infrared light loss per pass to second-harmonic generation, which will be discussed in detail in chapter 4.

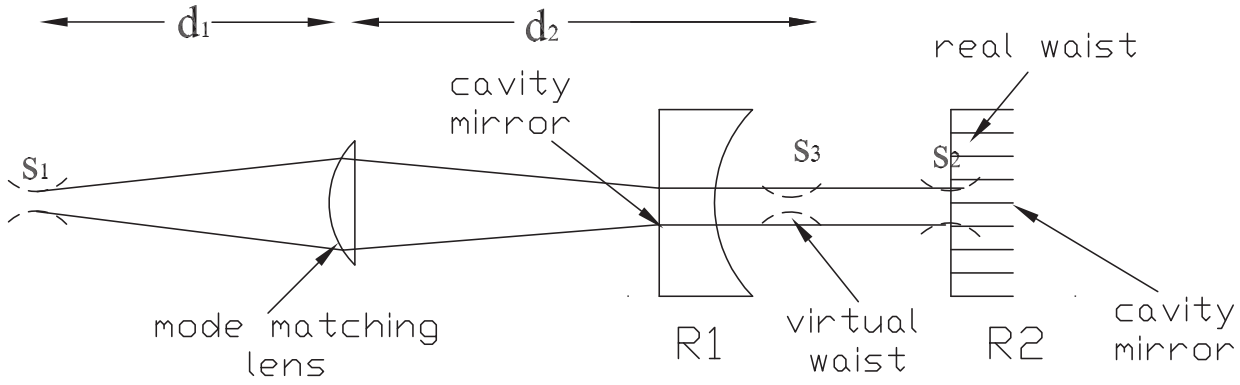

Figure 3.1 Our optical resonator consists of two mirrors separated by a distance L. One is the curved input coupler with radius $R1$. The other is flat, the high reflector, with $R2 = \infty$. A beam with waist s_1 passes through a coupling lens of selected focal length f and enters the optical cavity. The parameter s_2 is the minimum beam size inside the optical resonator. The virtual waist s_3, is the beam waist that corresponds to the beam emerging from the cavity.

3.2 General Set-up

Figure 3.1 illustrates our set-up of a optical resonator. Typically, an optical resonator consists of two mirrors with radius of curvatures $R1$ and $R2$ (we specialize $R_2 = \infty$) separated by a distance L. Light from an external laser enters the cavity through one of the two cavity mirrors (input coupler mirror), which is ideally designed to be partially reflecting such that its transmission loss is equal to the sum of all other losses in the system. The lens shown in Figure 3.1 is used to match the beam parameters from an external laser source into that of the optical resonator. The terms s_1 and s_2 are the minimum beam sizes (beam waist) of light from external laser source and inside the cavity respectively. The parameters d_1 and d_2 are the distances of the laser minimum beam size and virtual minimum beam size with respect to the lens. The term s_3 is the virtual waist of the beam, or the waist as it appears emerging from the cavity.

3.3 Gaussian Modes

Following [11], the electric field component for laser light travelling in the z direction can be written as

$$u = \psi(x, y, z) \exp(-jkz) \tag{3.2}$$

where ψ is the transverse electric field pattern of the laser beam. The wave equation in cylindrical coordinates that describes these modes is the following:

$$\frac{1}{r}\frac{\partial}{\partial r} r \frac{\partial \psi}{\partial r} - j2k_c \frac{\partial \psi}{\partial z} = 0, \tag{3.3}$$

where k_c is the vacuum wave vector. There are many solutions to the above equation having different transverse modes (spatial patterns). The lowest order transverse mode of equation 3.3 is called the TEM_{00} or Gaussian mode and is ubiquitous in laser systems used for atomic physics research. This mode is circular in its transverse dimension, and has very nice focusing properties. Mathematically, it is expressed as

$$\psi = \exp[-j(P(z) + \frac{kr^2}{2q(z)})], \tag{3.4}$$

where $q(z)$ is the confocal parameter, describing the variation in beam intensity with distance from the optical axis, and $P(z)$ is the complex phase shift. These two parameters are defined as the following:

$$\frac{1}{q(z)} = \frac{1}{R(z)} - \frac{j\lambda_0}{\pi s(z)^2}, \tag{3.5}$$

$$P(z) = (kz - \Phi). \tag{3.6}$$

where $s(z) = \sqrt{s_o^2[1 + (\frac{\lambda z}{\pi s_o^2})^2]}$ is the $1/e^2$ intensity radius or spot size of the gaussian beam, $R(z) = z[1 + (\frac{\pi s_o^2}{\lambda z})^2]$ is the wavefront radius of curvature, and $\Phi = \arctan(\frac{\lambda z}{\pi s_o^2})$ represents a phase shift difference between an ideal plane wave and Gaussian beam. The quantity s_0 in the expression for $s(z)$, $R(z)$, and $\Phi(z)$ is the beam waist. Following from equations 3.2 - 3.6, the gaussian beam transverse intensity pattern is written as:

$$I(x, y, z) = \frac{2P}{\pi s(z)^2} \exp[\frac{-2(x^2 + y^2)}{s(z)^2}], \tag{3.7}$$

where P is the power of the laser beam.

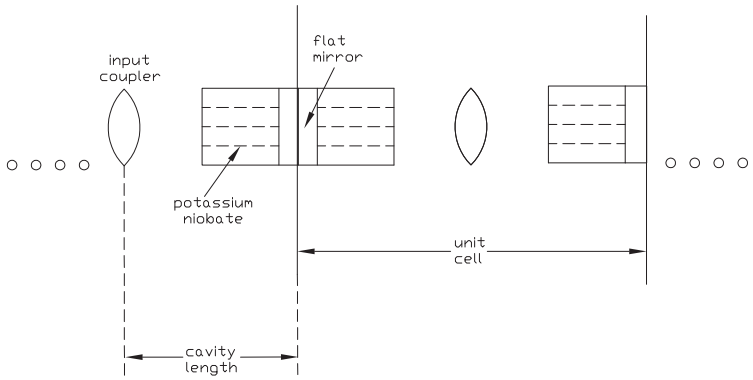

Figure 3.2 A lens system equivalent to the optical resonator used in our set-up, which consists of a concave mirror, a flat mirror, and $KNbO_3$ crystal.

3.4 Modelling Gaussian Modes in an Optical Resonator

Enhancement in an optical resonator of the TEM_{00} mode from an external laser source requires that the mode of the external laser be congruent to the mode emerging from the cavity. Thus, we need to know the beam profile of the external laser source and the beam profile of the mode in the cavity.

For our applications, we determine the beam profile of the lowest-order resonator mode (TEM_{00}), since it is easiest to match the laser profile into this mode and this mode leads to the highest nonlinear efficiency. We determine the profile of this mode by modelling the optical resonator as a periodic sequence of lenses (Fig. 3.2). The focal lengths of the lenses in the model are the focal length $f = R/2$, where R is the radius of curvature of a resonator curved mirror.

The confocal parameter $q(z)$ of a gaussian mode transforms through any optical system according to the ABCD law of ray optics [12]. Particularly, the confocal parameters $q_1(z)$ and $q_2(z)$ before and after an optical element are related by the following equation:

$$q_2(z) = \frac{Aq_1(z) + B}{Cq_1(z) + D}, \tag{3.8}$$

where A, B, C, and D are the entries of the ABCD matrix or ray for the optical elements. Using this rule, we can determine the beam radius of curvature and spot-

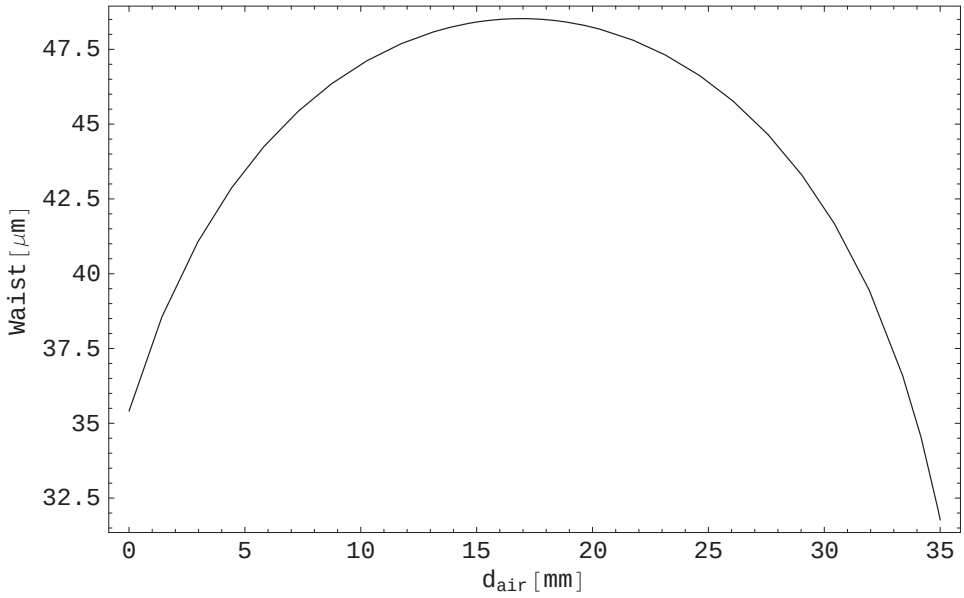

Figure 3.3 This is a plot of the beam waist of our resonator versus d_{air}, the distance between curved mirror and front face of the crystal for $R1 = 40$ mm, $n_{crystal} = 2.25$, and $d_{crystal} = 7$ mm.

size inside the optical resonator, by requiring that the confocal parameter $q(z)$ be the same after a round trip in the cavity.

For our model (Figure 3.2), the ABCD matrices $\left(\begin{smallmatrix} A & B \\ C & D \end{smallmatrix}\right)$ that we need to describe our system are given by:

$$T_{distance} = \begin{pmatrix} 1 & \frac{d}{n} \\ 0 & 1 \end{pmatrix}, \tag{3.9}$$

and

$$T_{lens} = \begin{pmatrix} 1 & 0 \\ -\frac{2}{R} & 1 \end{pmatrix}, \tag{3.10}$$

where $T_{distance}$ is the transfer matrix that describes the transformation over a meduim of length d and index n. T_{lens} is an ABCD matrix that describes the transfer of a beam through a thin lens of focal length f.

The resultant ABCD matrix is found by applying the transfer matrices of Eq. 3.9 - 3.10 in the reverse order to the propagating beam through the unit cell given in Fig. 3.2. From this the resultant ABCD matrix is the following:

$$\begin{pmatrix} A & B \\ C & D \end{pmatrix} = \begin{pmatrix} 1 & \frac{d_{crystal}}{n_{crystal}} \\ 0 & 1 \end{pmatrix} \begin{pmatrix} 1 & \frac{d_{air}}{n_{air}} \\ 0 & 1 \end{pmatrix} \begin{pmatrix} 1 & 0 \\ \frac{-2}{R1} & 1 \end{pmatrix} \begin{pmatrix} 1 & \frac{d_{air}}{n_{air}} \\ 0 & 1 \end{pmatrix} \begin{pmatrix} 1 & \frac{d_{crystal}}{n_{crystal}} \\ 0 & 1 \end{pmatrix}$$

$$= \begin{pmatrix} 1 - \frac{2(\frac{d_{air}}{n_{air}} + \frac{d_{crystal}}{n_{crystal}})}{R1} & \frac{2(d_{crystal}n_{air} + d_{air}n_{crystal})(d_{crystal}n_{air} + n_{crystal}(d_{air} - n_{air}R1))}{n_{air}^2 n_{crystal}^2 R1} \\ -\frac{2}{R1} & 1 - \frac{2d_{air}}{n_{air}R1} - \frac{2d_{crystal}}{n_{crystal}R1} \end{pmatrix} \quad (3.11)$$

where $d_{crystal}$ is the crystal length, n_{air} and $n_{crystal}$ is the air and crystal index of refraction respectively, and d_{air} is the distance from the input coupler to front-face of crystal.

By setting $q_1(z) = q_2(z)$ in Eq. 3.8 and using the ABCD elements of Eq. 3.11 we obtain the following expression for the resonator beam waist

$$s_2^2 = \frac{2\lambda B}{\pi\sqrt{4 - (A + D)^2}}, \quad (3.12)$$

and it is by symmetry located at the flat mirror (The beam waist is at the location that corresponds to $R(z) = \infty$.). Figure 3.3 is a plot of Eq. 3.12 (resonator beam waist) as a function of d_{air}, the distance between the curved mirror and front face of the crystal.

3.5 Longitudinal Modes

The build-up of a transverse mode in a given optical resonator can only occur at certain frequencies. This discrete set of resonance frequencies are the longitudinal (axial) electromagnetic modes of the optical resonator. The frequency of these modes are determined by the resonance condition that the round-trip phase shift of the resonator mode must be an integer multiple of 2π. This is mathematically expressed as:

$$\frac{4\pi\nu L}{c} - \theta_{nm} = 2\pi p, \quad (3.13)$$

where the term $\frac{4\pi\nu L}{c}$ is the axial mode phase shift, and p is the axial mode integer. The term θ_{nm} is the transverse mode phase shift having mode integers n and m, which

varies for different modes. The resonance frequencies obtained from Eq. 3.13 are the following:

$$\nu_{pnm} = p\frac{c}{2L} + \frac{\theta_{nm}c}{4\pi L} \tag{3.14}$$

where L is the cavity length and c is the speed of light in vacuum. In Eq. 3.14 $\frac{c}{2L}$ is the free-spectral range (FSR) of the optical resonator, which is the frequency separation between adjacent TEM_{00} longitudinal modes in Hz. The transverse mode spectrum is described by the term $\frac{\theta_{nm}c}{4\pi L}$ and will be illustrated and briefly discussed in Chapter 4.

3.6 Resonator Losses

The frequency criterion for optical waves to exist inside a resonator is relaxed, when the resonator has losses [13], for example, when the mirrors are not perfect reflectors. The losses of a cavity are describe by the finesse $\mathcal{F}$, which is expressed in terms of the overall losses in the system α as:

$$\mathcal{F} = \frac{\pi \exp[-\alpha]D}{1 - \exp[-2\alpha]D} \simeq \frac{2\pi}{\alpha D}, \tag{3.15}$$

where α is given by

$$\alpha D = \ell + C + \ln\frac{1}{R_a R_b}, \tag{3.16}$$

where ℓ is the round-trip parasitic loss and C is the infrared blue conversion loss. The term $\ln\frac{1}{R_a R_b}$ is losses due to mirror reflectivities. For $R_b \simeq 1$ Eq. 3.15 reduces to the following:

$$\mathcal{F} \simeq \frac{2\pi}{\ell + C + T_a}, \tag{3.17}$$

where $T_a \simeq 1 - \mathrm{R}_a$ is transmission of the input coupler mirror. In the presence of these the modes are no longer discrete sharp peaks as a function of frequency, but have a spectral full-width-half-maximum (FWHM) Γ given by:

$$\Gamma = \frac{FSR}{\mathcal{F}}. \tag{3.18}$$

Chapter 4
Experimental Details

This chapter discusses the experimental layout, the optical resonator design, and the experimental procedure used to convert light at 844 nm to 422 nm.

4.1 Experimental Apparatus

The experimental set-up used to produce light at 422 nm is displayed in Figure 4.1 and Figure 4.2. In Fig. 4.1, p-polarized light is emitted from a Toptica single frequency high powered tunable diode laser and coupled into a optical fiber. The output light from the fiber ranges in power from 10-120 mW and has a virtual beam waist of 82.9 μm located approximately 12 cm behind the output fiber head.

The light from the fiber passes through an $f = 200$ mm focal length lens (for mode matching), and a dichroic mirror, before passing into the optical resonator. The optical resonator is semi-monolithic, consisting of an input coupling mirror and a $KNbO_3$ crystal. The input coupler mirror, which is mounted on a piezo-electric transducer (PZT) to adjust the cavity length, has radius of curvature of 40 mm, transmits 5% at 844 nm and 90% at 422 nm, and serves as a output coupler for the blue. The $KNbO_3$ crystal is 7 mm in length and is "a-cut", which means the principal axes of the crystal is oriented such that the fundamental light propagates along the crystal's a-axis with its polarization along its b-axis. The end faces of the crystal are flat. The front interface is anti-reflection coated for the 844 nm and 422 nm light. The crystal back face serves as the mirror and it is dielectrically coated as a high reflector with reflectivity of .999 for light at 844 nm and 422 nm (Fig. 4.3).

The $KNbO_3$ crystal is wrapped in indium foiled and resides inside an aluminum enclosure (not shown). This enclosure sets on top of two cascaded Thorlabs 3-6 amp thermo-electric coolers for active control of the crystal temperature. In turn,

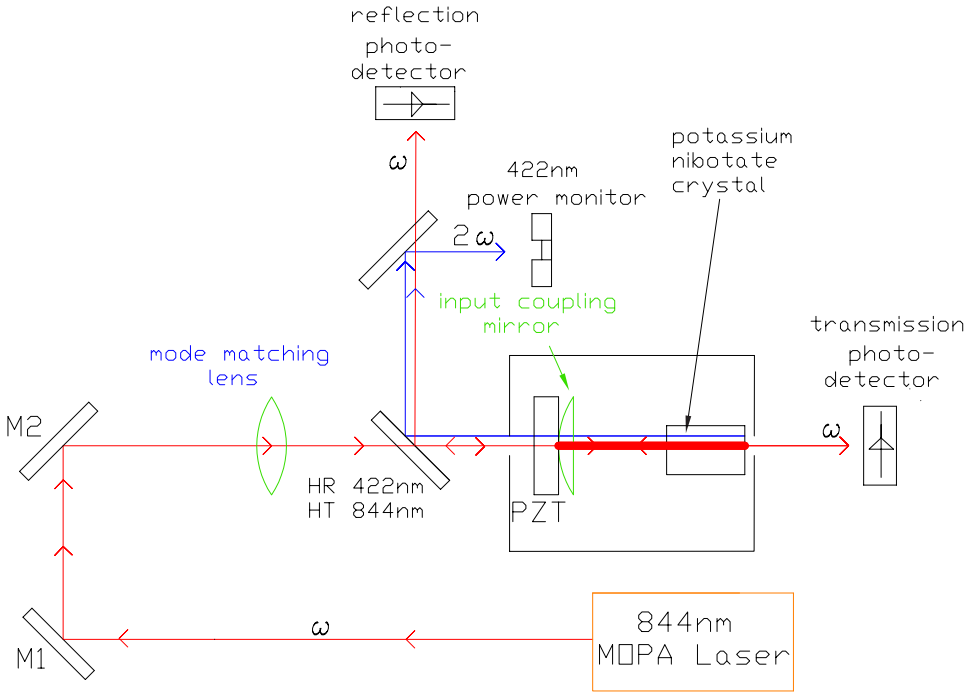

Figure 4.1 Schematic of the experimental configuration (not to scale). HR, high reflector, HT, high transmission.

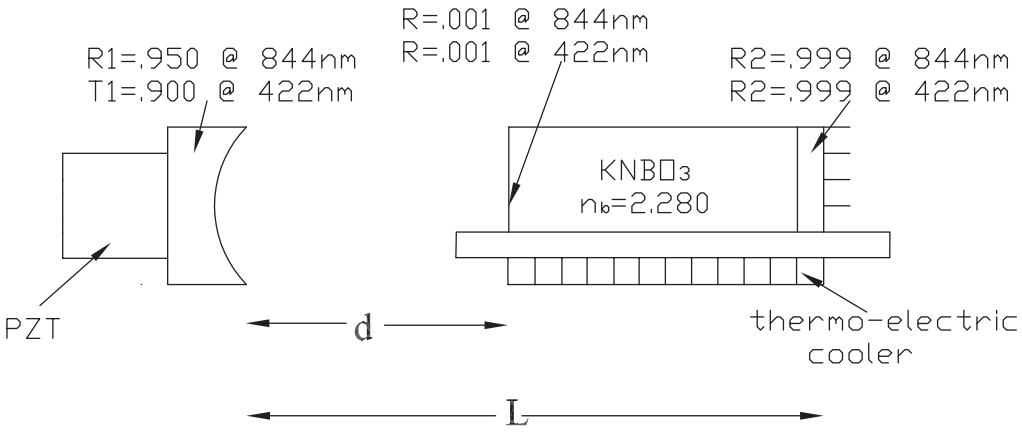

Figure 4.2 The crystal-mirror arrangement used in our system.

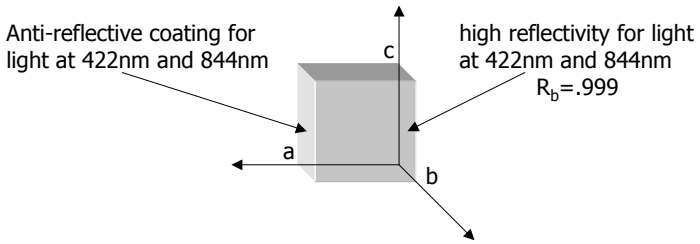

- d_{eff} = -21 pm/V, a=7mm, b=3mm, c=3mm
- biaxial crystal; $n_a \neq n_b \neq n_c$
- cut for temperature tuned noncritical type I phase matching at room temperature

Figure 4.3 This is a pictorial illustration of our potassium niobate crystal(not to scale).

the thermo-electric cooling configuration resides on top of a copper kinematic mount constructed in our machine shop, which is used for aligning. In addition, the copper mount serves as a heat sink, and it transfers heat generated from the thermo-electric coolers out of the system.

Both input coupler stage and the $KNbO_3$ stage are kept inside of an aluminum box. This housing is hermitically sealed and filled with O_2 in order to prevent H_2O condensation during cooling, and to alleviate the long term effects of humidity on the crystal. Light is allowed to enter and leave the housing via windows that are slightly angled to eliminate etalon affects. The reflected and transmitted IR light from the optical resonator are collected on Thorlabs photo-diodes, and the cavity mode spectrum is displayed on an oscilloscope.

4.2 Mode Matching

When the fundamental beam parameters of the cavity and the external laser source are known, the gaussian modes of the laser source and optical resonator can be matched. If the modes of the two systems are not matched, the TEM_{00} mode output of the external laser source will couple into several transverse modes of the

cavity, which will limit the enhancement of the external laser's fundamental mode. Thus, to prevent the excitement of additional resonator modes, a lens is used to transform the TEM_{00} from the laser into that of the cavity. This phenomena is known as mode matching.

In general, to mode match, only the sizes and positions of the beam waists of both systems need to be known. Once that information is at hand, the problem is to determine the focal length and the distances from each waist to the lens that are needed to match the two systems, as illustrated in Figure 3.1.

In practice, the input-coupler mirror of the optical resonator is a fused silica substrate. This substrate acts as a plano-concave lens of focal length $-2R_{mirror}$, where R_{mirror} is the radius of curvature of the input coupler. This effect, in turn, causes the waist size and location for the beam that emerges from the cavity to be different from that of the resonator. Therefore, in order to properly mode match we must take into consideration this lens action, and determine the size, s_3, and location of this virtual beam waist [12].

We determined the size of the virtual beam waist using the following equation [15]:

$$s_3 = \frac{f\lambda}{\pi S}[(1 - \frac{f_{lens}}{R})^2 + (\frac{\lambda f_{lens}}{\pi S^2})^2]^{-\frac{1}{2}}, \tag{4.1}$$

where S and R are the beam spot size and radius of curvature of the resonator mode at the location of the input coupler. The term f_{lens} is the focal length of the input coupler substrate. Figure 4.4 is a plot of the virtual waist of our system as a function of spacing d_{air} between the input coupler and doubling crystal. For our experimental configuration, the chosen distance between the front-face of the doubler crystal and the input coupler mirror (d_{air} = 25.9 mm) results in a virtual waist s_3 of 29.0 μm and a resonator beam waist s_2 of 45.9 μm.

The size of the resonator beam waist is critical in frequency doubling experiments, since the harmonic power, losses (BLIRA), and other mechanisms such as thermal

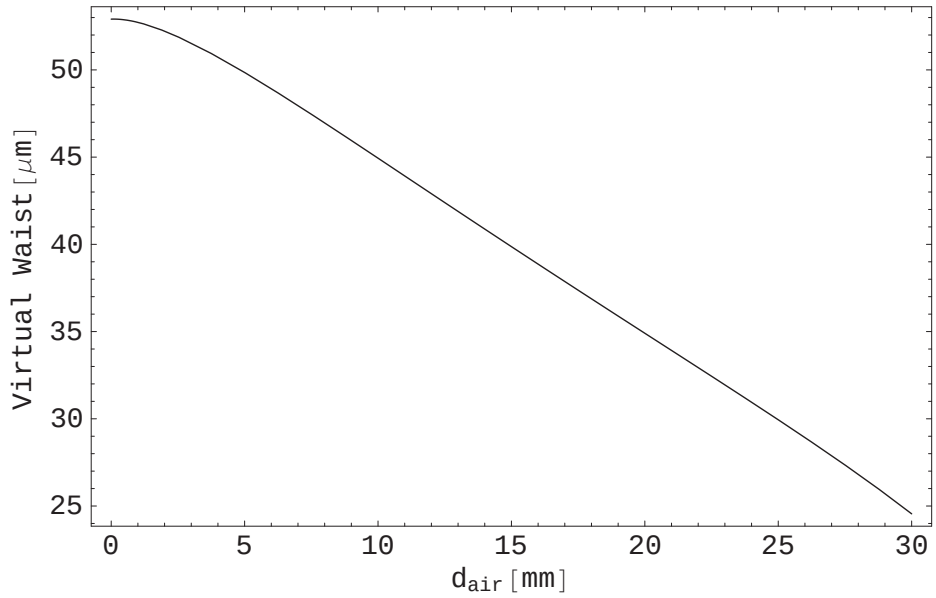

Figure 4.4 Virtual waist as a function of spacing d_{air} between the input coupler and doubling crystal.

lensing depend on it (See Section 4.8). For instance, Eq. 2.2 shows that ξ_{nL} is inversely proportional to the beam area ($A = \pi s_2^2$). Thus, the smaller the beam area the larger harmonic power. However, as will be shown in sections 4.7 and 4.8 of this thesis, smaller values of the beam waist can result in larger losses and cause other effects that limit the amount of harmonic power.

The location of the virtual waist is given by the z solution to the equation

$$R_3 = z[1 + (\frac{\pi s_3^2}{\lambda z})^2], \tag{4.2}$$

where $R_3 = \frac{1}{\frac{1}{R} - \frac{1}{f_{lens}}}$ is the radius of curvature of the virtual beam at the output of the input coupler substrate. The position of the virtual waist versus the spacing d_{air} is shown in Figure 4.5. For the value $d_{air} = 25.9$ mm used in our experiment, we determined the location of the virtual waist to be 26.2 mm behind the input coupler.

The lens used to mode match the beams must have a focal length f that is greater

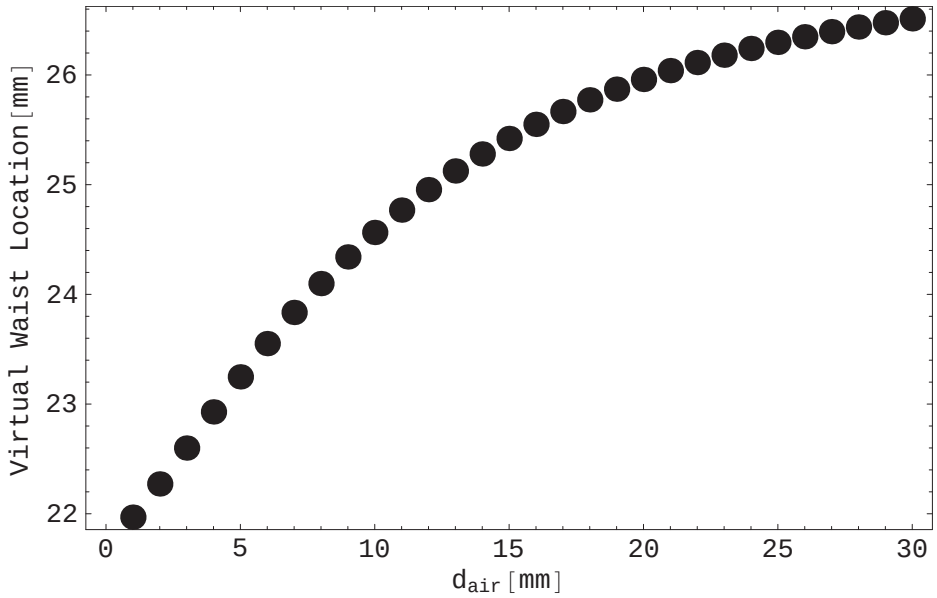

Figure 4.5 Virtual waist position as a function of spacing d_{air} between the input coupler and front-face of the doubling crystal. The location is with respect to the input coupler.

than the characteristic mode matching length given by [11]:

$$f_o = \frac{\pi s_1 s_3}{\lambda}, \tag{4.3}$$

where s_1 is the input laser beam waist and s_3 is the virtual waist.

The distances of the waists for both systems from the mode matching lens were determined using the following equations:

$$d_1 = f \pm \frac{s_1}{s_3}\sqrt{f^2 - f_o^2}, \tag{4.4}$$

and

$$d_2 = f \pm \frac{s_3}{s_1}\sqrt{f^2 - f_o^2}. \tag{4.5}$$

From these equations we found our distances to be $d_1 = .977$ m and $d_2 = .248$ m.

4.3 Cavity Alignment

We begin to align our system by positioning our mode matching lens and doubling crystal so that the infrared beam passes through their centers, and its reflection off the

back cavity mirror overlaps with the incident beam. Then we place the input coupler mirror, which is attached to a PZT and mounted on to an optical mount, into the system and adjusted it such that the reflection beam from the input coupler overlaps with the input beam of the laser. Next, we modulated the PZT, and transmission of the TEM_{00} cavity mode along with many other higher order cavity modes through the back-face of the crystal were visible on the output from the photo-diode. Finally, we adjust the input coupler mirror, the doubler crystal, and mirrors M1 and M2 in Fig. 4.1 to couple most of the power into the TEM_{00} mode.

4.4 Cavity Modes

In our experimental configuration we use our optical resonator as a scanning interferometer in order to monitor the mode spectra. As we scan the length of our cavity, when the laser sequentially comes into resonance with a cavity longitudinal mode, light enters the cavity, and excites the cavity modes. Mathematically, the laser-cavity resonance condition for two adjacent modes is expressed as:

$$f_l = \frac{pc}{2L} = \frac{(p+1)c}{2(L+\Delta L)} \tag{4.6}$$

where f_l is the laser frequency, p is the axial mode number, and $\Delta L = \alpha \Delta V$ is the change in cavity length (corresponding to a FSR) in terms of a change in PZT voltage ΔV. The term α is the PZT voltage to length proportionality constant.

Figure 4.6 is the mode spectrum of our optical resonator. The large sharp peaks, p and $(p+1)$, are the TEM_{00} of the cavity, which are separated by 1FSR ($\Delta V \simeq$100V). The next taller peaks is are higher-order transverse modes, which are shifted from the fundamental modes by $\frac{1}{4}$ FSR. From the figure we estimated that more than 90% of the external laser power is coupled into the gaussian mode of the resonator.

We measured the separation of the p and $(p+1)$ cavity modes by turning off the PZT scan, and scanning our 844 nm laser frequency. Now, we scan our laser frequency such that it will sequentially come into resonance with the cavity. While

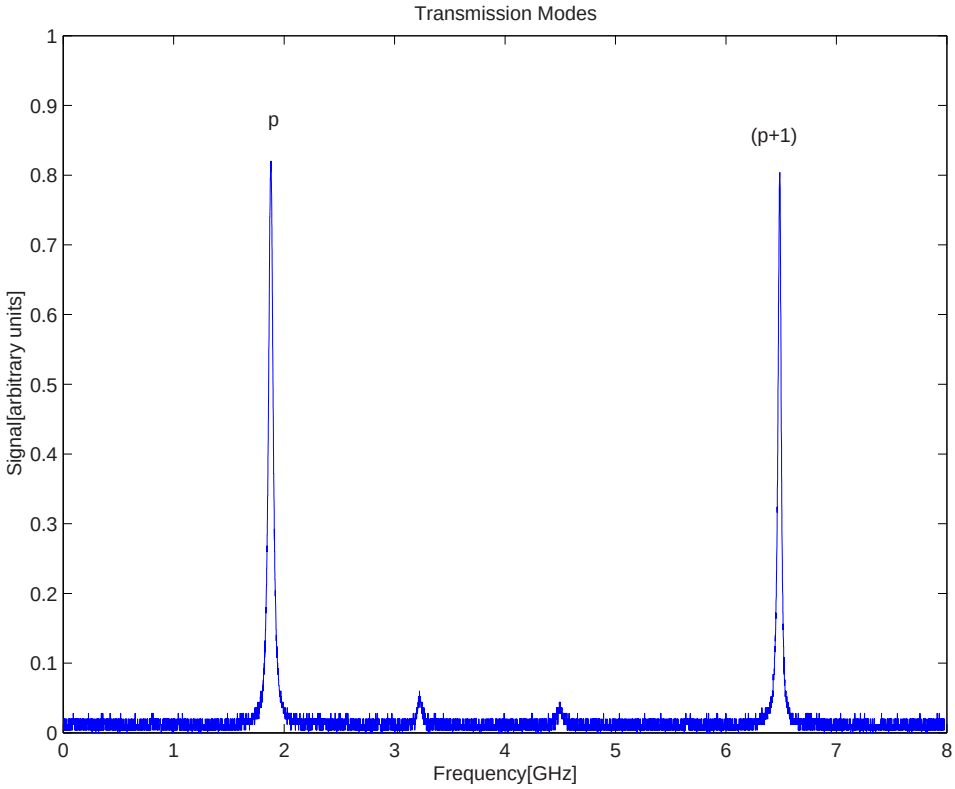

Figure 4.6 Mode spectrum of 844 nm IR enhancement cavity, with fit function.

doing this, we monitor, using a Burleigh WA-1000 wavemeter, the laser frequencies that correspond to adjacent cavity resonances. Using this procedure, we measure the FSR of our optical resonator to be 4.4 GHz ±.1 MHz, where .1 MHz is the resolution of our wavemeter. This matches well with the value calculated from Eq. 3.14 of 4.56 GHz.

Next, we determined the FWHM of our system by scanning the cavity length and fitting a single transmission lineshape (Fig. 4.7) to a Lorenzian (Blue light is not being generated for this measurement.):

$$P(\nu) = \frac{P_o}{1 + 4(\frac{\nu - \nu_o}{\Gamma})^2}, \tag{4.7}$$

where ν_o is the resonant frequency of the cavity, Γ is the full width at half-maximum, and P_o is the infrared power at the peak of the Lorenzian. From this fit we determined our FWHM to be 46.5 MHz. This implies a finesse $\mathcal{F}$ of our cavity of 105.5 ($\mathcal{F} = \frac{FSR}{FWHM}$).

Using equation 3.13, and the cavity mirror reflectivities $R_a = .95$ and $R_b = .999$ (These values are specified by the manufacturer), and the value of finesse obtained from the fit, we were able to determine the parasitic loss ℓ (loss other than mirror reflectivities away from phase matching) in our system to be 1.4%. We expect this loss is most likely due to $KNbO_3$ absorbing and scattering the infrared light.

4.5 Temperature Tuning

Light at 422 nm is produced by means of temperature-tuned non-critical type I phase matching. At $\sim 21°C$, we visibly see 422 nm light emitted from the cavity. It is separated from the fundamental light via a dichroic beam splitter that is dielectrically coated for high reflection of s-polarization at 422nm and low reflection for p-polarization at 844 nm.

Figure 4.8 is a plot of the harmonic power (in the locked state) versus temperature for an input infrared power of 70 mW. The PZT for these measurements was controlled

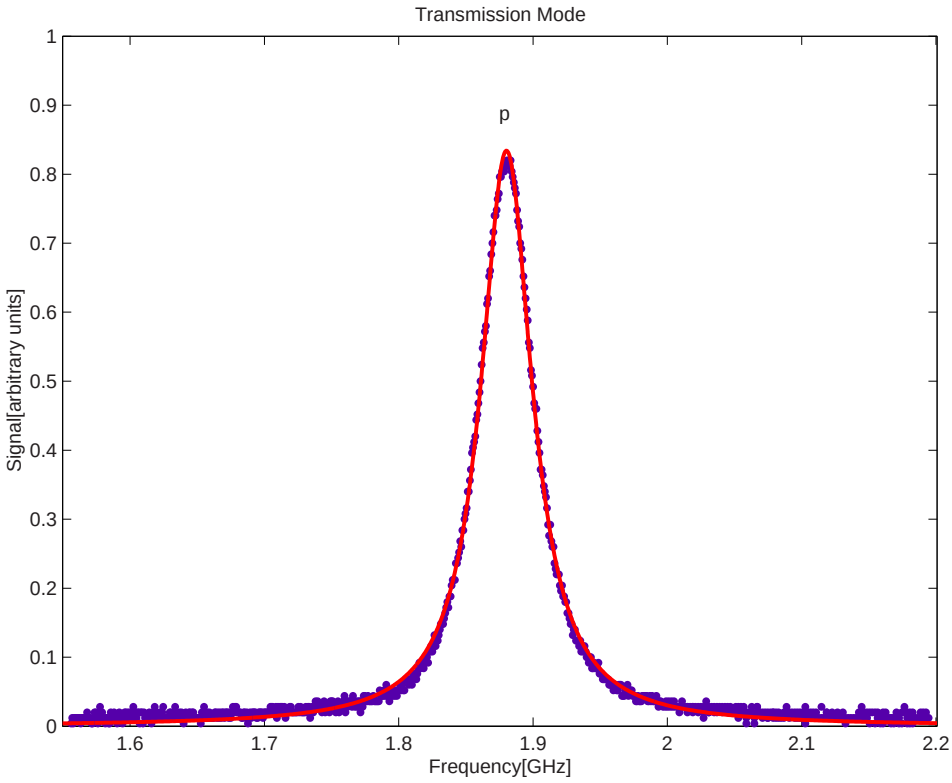

Figure 4.7 This is a plot of an single transmission mode of the 844 nm IR enhancement cavity, with fit function.

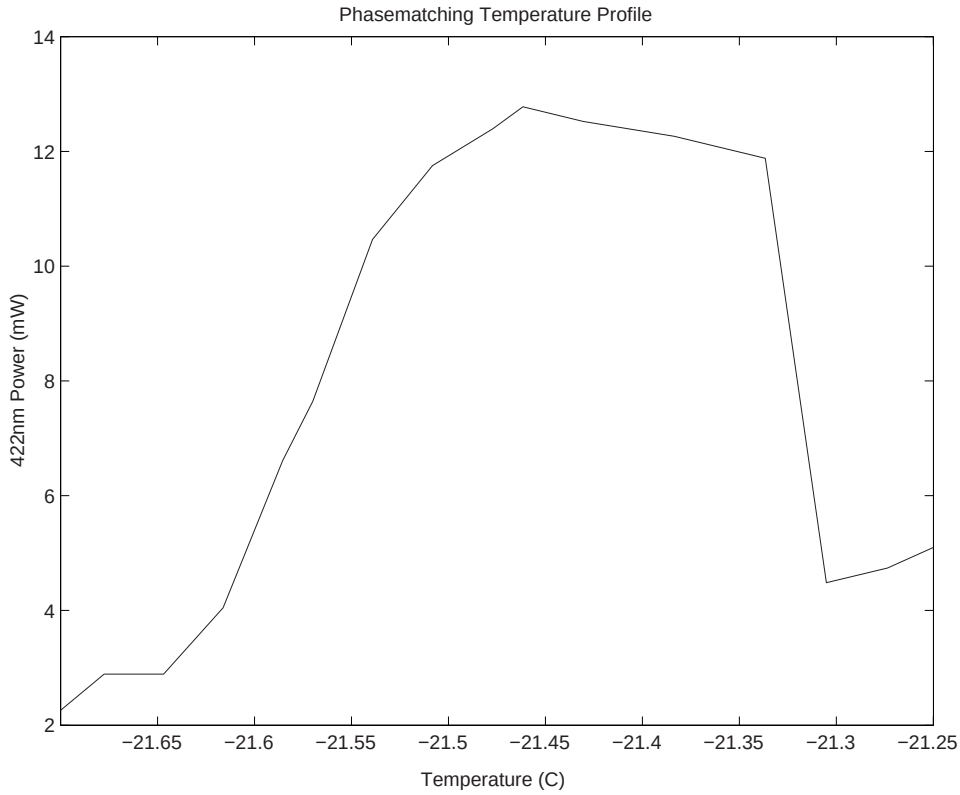

Figure 4.8 This is the temperature tuning curve for our blue laser source having an input infrared power of 70 mW.

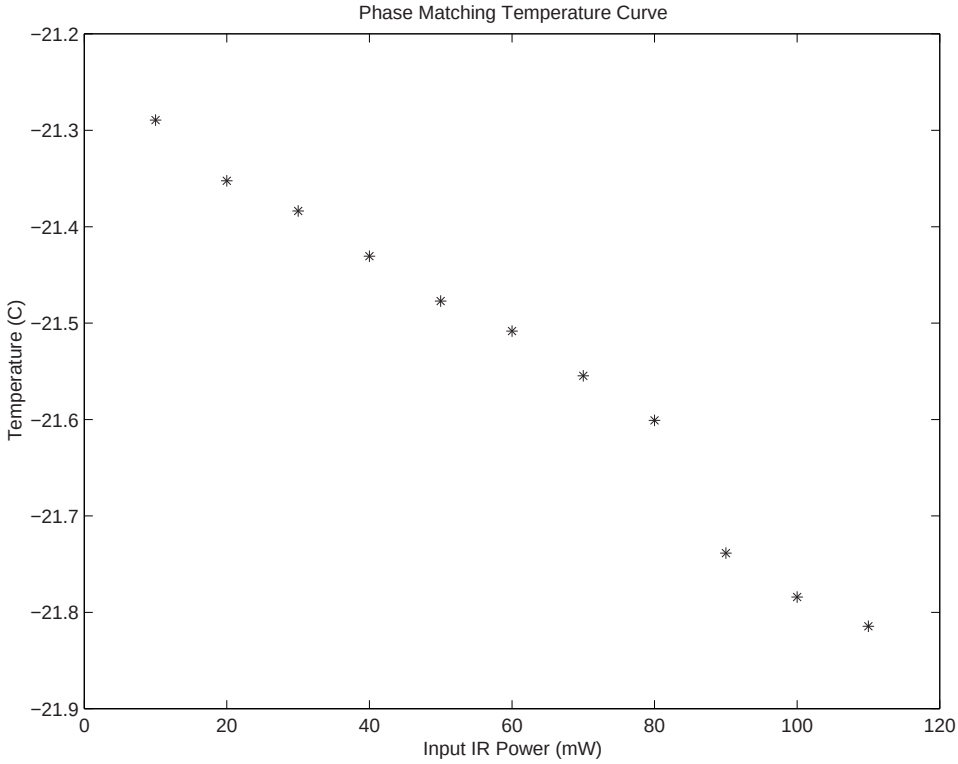

Figure 4.9 The optimal phase-matching temperature increases with larger incident power. This response is due to the heating of the crystal as a result of more circulating power in the cavity.

such that its length always corresponds to maximal build-up inside the cavity. In this locked state of the cavity, for 70 mW of fundamental power, the maximum blue power occurred at a temperature of $-21.47°C$. This is close to the value of $-20°C$ estimated from the graph given in [8]. We took the temperature bandwidth for phase matching in our configuration as the FWHM of this peak, which is $\sim .3°C$. Using Eq. 4.6 [9]

$$\Delta T = \frac{.443\lambda_1}{L\|\frac{\partial n_b}{\partial T} - \frac{\partial n_c}{\partial T}\|}, \tag{4.8}$$

where $\frac{\partial n_b}{\partial T} = -3.3 \times 10^{-5}$ and $\frac{\partial n_c}{\partial T} = 1.3 \times 10^{-4}$ are the thermo-optic coefficients of $KNbO_3$ and λ_1 is the fundamental wavelength. We calculated the value of the temperature bandwidth to be $.324°C$. This value agrees well with our measurement.

Figure 4.9 is a plot of the phase-matching temperature vs. input fundamental

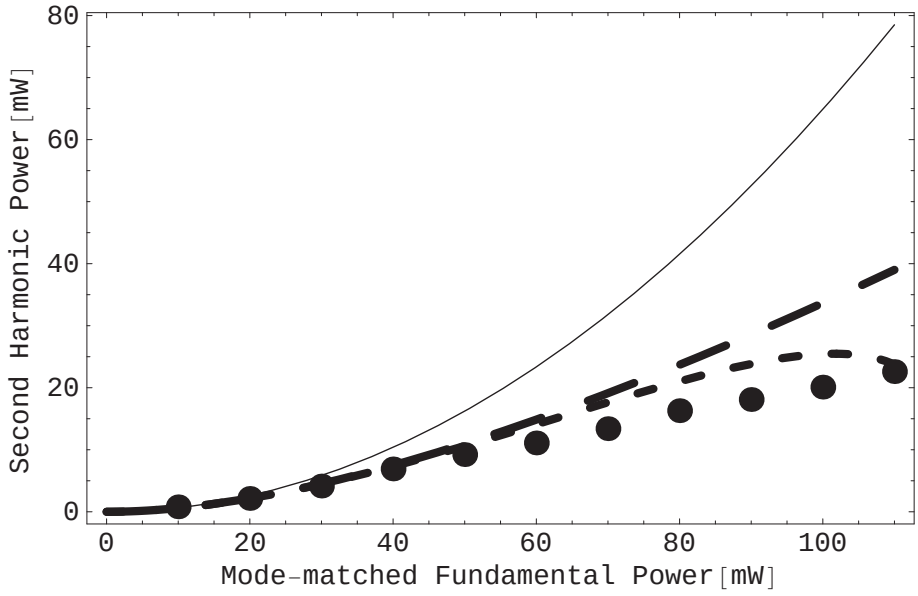

Figure 4.10 Generated second-harmonic power as a function of the mode-matched fundamental power. The solid, long-dashed, and short-dashed curves are obtained from theory. Filled circles are data.

power. This figure shows the decrease in phase-matching temperature with increase in infrared power. This trend is due to absorption, since as the fundamental power increases more infrared power and blue power is absorbed by the crystal, thereby causing it to heat-up. Thus, in order to phase match the crystal with the additional heat, the temperature of the housing must be decreased to lower values.

4.6 Frequency Doubling

Figure 4.10 is a plot of the harmonic power at 422 nm as a function of the fundamental mode-matched power. The filled circles represent the measurements of the second-harmonic power corrected for transmission losses from the output of the crystal to the blue detector. For a maximum fundamental power of 110 mW out of our fiber, of which we estimate 83% is optimally coupled into the fundamental mode, we get a peak second-harmonic power (locked) of 22.6 mW in a single longitudinal mode. After a series of optical elements, i.e., input coupler mirror, dichroic mirrors,

and windows, only 19.24 mW is usable. The solid curve is a fit by eye of the equation

$$P_{2\omega} = \xi_{nL} P_c^2, \tag{4.9}$$

to the data with setting the infrared to blue conversion loss to zero (C=0). The value of ξ_{nL} from Eq. 4.9 was varied for the fit and we found it to be best at .004/W. For mode-matched fundamental powers up to 20 mW, there is good agreement with experiment. However, for input powers greater than 20 mW, we could not get a good fit. Deviations in experiment and theory begin to increase because the second-harmonic conversion loss starts to significantly reduce the circulating power (see Appendix A). Therefore, making C=0 in Eq. 3.1 is a bad approximation in this power regime.

The long-dashed curve is a fit including the effect of infrared conversion loss in Eq. 4.9. For fundamental powers as great as 40 mW there is good agreement with theory. As the input power levels increase, inconsistencies between experiment and theory begin to occur, which indicates other effects must be important.

The short-dashed curve in Fig. 4.10 is a fit including both the effects of IBCL and thermal lensing. Thermal lensing is due to thermal gradients in $KNBO_3$, which severely causes the beam waist to expand inside the crystal. Thermal lensing is complicated to model, so the fit we obtain was not great, however it did reproduce the trend of second harmonic power not increasing quadratically with input power, so we suspect this is a problem.

Figure 4.11 is a plot of the optical-to-optical conversion efficiency as a function of incident power. The peak conversion efficiency for our set-up is 24.75 %, which is much less than maximum efficiencies of 60% in experiments done in [17]. The higher conversion efficiency obtained in [17] is a result of having a longer harmonic wavelength and using a ring cavity configuration. In $KNbO_3$, absorption increases with decreasing wavelength. For a ring cavity, build-up is via a single direction travelling wave. The advantage of this is that the cavity no longer posses standing waves to cause spatial heating. Spatial heating is the heating of a specific region in

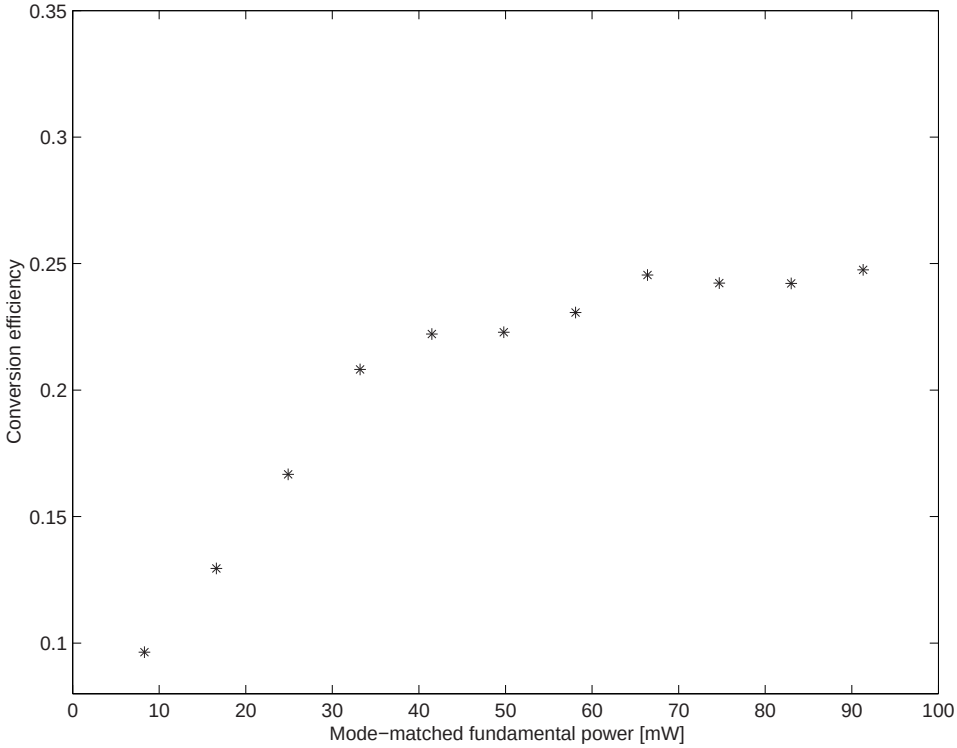

Figure 4.11 Conversion efficiency as a function of mode-matched fundamental power. The asterisks are calculated from the measured harmonic output power.

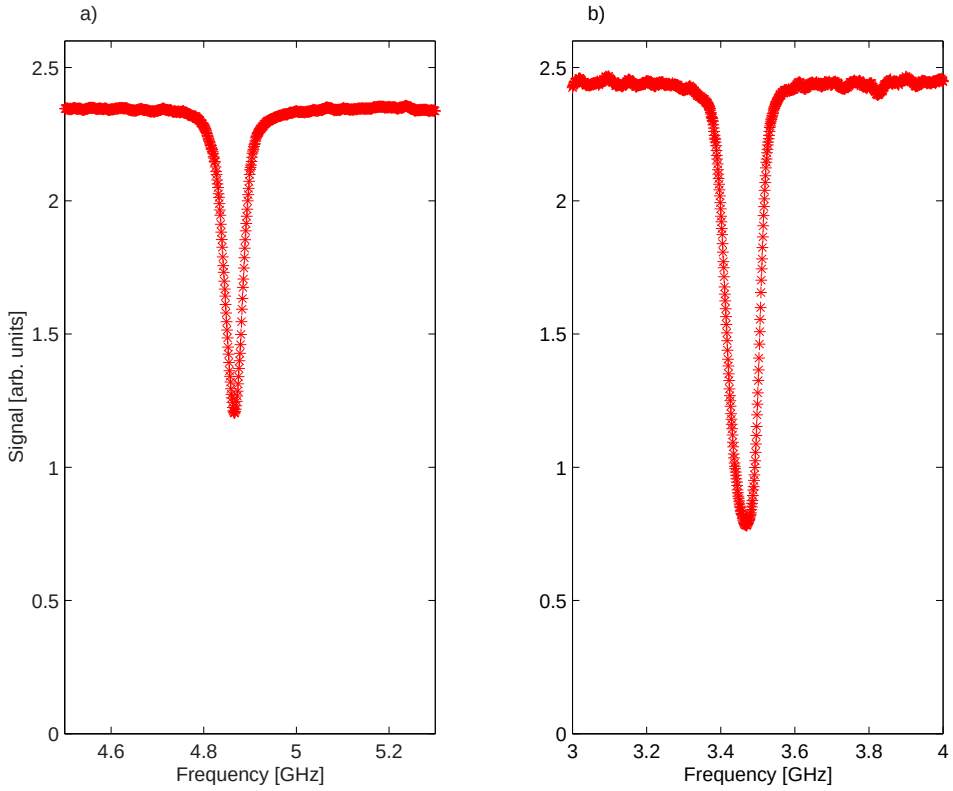

Figure 4.12 Reflection mode spectrum of 844 nm IR enhancement cavity. (a) Cavity reflection mode taken with 70 mW of incident IR power when not phased matched. (b) Reflection lineshape taken with 70 mW of incident IR power when generating second-harmonic power at 422 nm.

the crystal due to presence of standing waves. This effect can take the crystal away from its optimal phase-matching temperature, thus reducing the harmonic output of the system.

4.7 Loss Mechanisms

From the analysis in section 4.6 we have shown that the performance of our blue laser source is limited by losses. Now we will study in detail the types of losses and different manners in which losses affect our system.

Losses have an affect on the amount of input power from the external laser accepted into the cavity. For instance, if the sum of the losses in the resonator, i.e.,

scattering, absorption, and infrared-to-blue conversion loss does not equal the transmission loss of the input coupler, then a fraction of the input light will reflect from the cavity. If the sum of the cavity losses equals to the input mirror transmission, then no light reflects from the cavity, and the optical resonator is said to be impedance matched [17]. Figure 4.12 is a study of impedance matching for our system.

Figure 4.12a shows the reflected signal from the input coupler mirror, when the crystal is far away from its phase-matching temperature. The only loss present under this condition is the parasitic loss, which has a value of 1.4%. For this case, 47.5% of the incident power is reflected from the cavity. However, in Fig. 4.12 b, which is the reflected signal from the cavity when the crystal is at phase-matching temperature, only 22.1% of the power is reflected. This percent change in reflected power is due to an increase in the losses of our system as we generate 422 nm light. Since, as we create blue light, the losses in the cavity increase, bringing our system closer to its impedance matched state. This value is reasonable since the sum of the losses we account for in our system i.e. parasitic loss, BLIRA, and infrared-to-blue conversion loss total to 2.5%, which is less than the input mirror transmission of 5%.

We deduced from Fig. 4.12b that the intra-cavity losses increase when generating blue light. The two loss mechanisms that influence our system in the phase-matching state is infrared-to-blue conversion loss and BLIRA. BLIRA is a phenomenon where $KNbO_3$ absorbs infrared light when it is illuminated with blue light.

The infrared-to-blue conversion loss per pass is given by following expression [21]:

$$C = \xi_{nL} P_c(P_{input}), \tag{4.10}$$

where P_c is function of P_{input}, the mode-matched fundamental power in the cavity.

Figure 4.13 is a plot of the infrared-to-blue conversion loss as a function of input power neglecting the effect of thermal lensing on the circulating power. The peak conversion loss occurs at an input power of .082 W and is $\sim$.8%. The behavior of the conversion loss is a result of the nonlinear relationship between the conversion loss

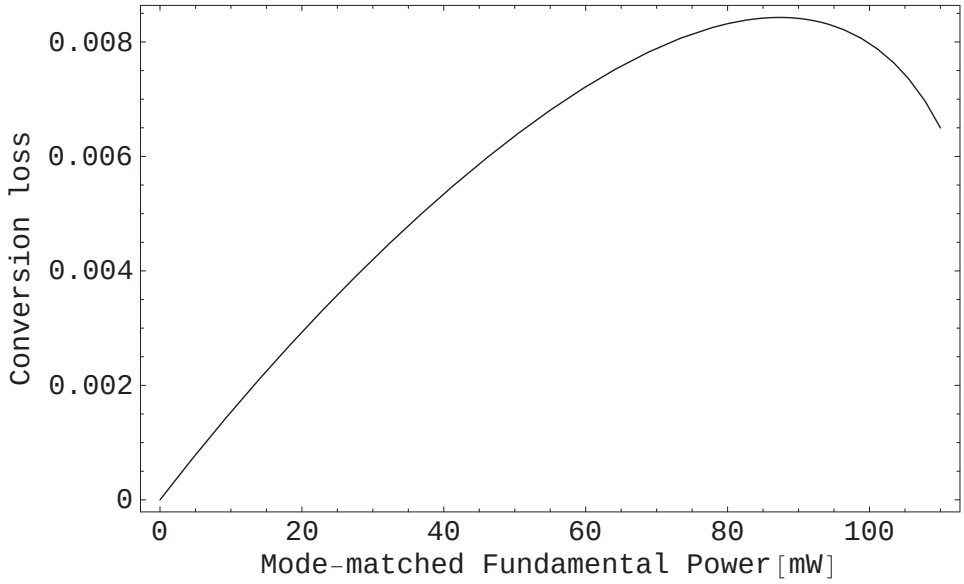

Figure 4.13 The infrared-to-blue conversion loss as a function of input mode matched fundamental power in the cavity

and circulating power. For $P_{input} < .06$ W the circulating power is approximately the enhancement factor, $\frac{(1-R_a)}{[1-\sqrt{R_a R_b(1-\ell+C)}]^2}$, which is essentially a constant value in this regime, multiplied by the input power. Therefore, the conversion loss increases linearly with P_{input}. However, as the input power exceeds .06 W the conversion loss increase becomes less with increasing P_{input} until it reaches its maximum value. Afterward, the conversion loss begins to significantly affect the enhancement factor, and the conversion loss starts to decrease with input power.

Following the expression for the absorbed power density and heat equation given in [21], we derived an expression for the fraction of power loss due to BLIRA, which is expressed as:

$$P_{BLIRA} = \int_V \frac{24 P_b P_{cir} \delta}{\pi^2 a^4 L^2} \exp(\frac{-6r^2}{a^2}) z^2 \, \mathrm{dV}. \tag{4.11}$$

The integrand in equation 4.11 is the IR power density absorbed due to BLIRA, where P_{cir} and P_b are the circulating and harmonic power. The variables a and L are the beam waist and crystal length, δ is the BLIRA absorption coefficient, and r is the

width of the crystal. We can approximate the crystal as a cylinder, since the beam area is much less than the square cross section of the crystal. Thus, integration can be done in cylindrical coordinates.

By integrating over a cylindrical volume we obtained the fraction of infrared power absorbed due to BLIRA. Thus, for our crystal dimensions $L = 7$ mm, $r = 1.5$ mm, and using the value of δ obtained in [22], for a maximum $P_{cir} = 3.5$ W and $P_b = 22.6$ mW, we determined our peak absorption fraction due to BLIRA to be .5%. This value is two times smaller than the value obtained in the experiment done in [17], which achieved a peak conversion efficiency 60%. This comparison along with the information obtained from fits in Fig. 4.13 suggests to us that BLIRA is not a significant limiting mechanism in our system. However, it does further support thermal lensing, since it implies that up to 20 mW of power is being absorbed by the crystal on axis, which would lead to development of thermal gradients inside the crystal, thereby causing it to behave as a lens.

4.8 Thermal Effects

Thermal effects can be very harmful to doubling efficiency. For instance, the absorbed light can cause transverse thermal gradients to arise inside the crystal. These gradients, in turn, give rise to a spatially dependent index of refraction $n(r)$, which produces a lens action called thermal lensing [23]. This effect modifies the beam waist within the crystal, which causes ξ_{nL} to decrease. Also, it reduces mode matching, mode quality, and affects the phase matching of the system.

We evaluated the effect of thermal lensing on our cavity beam waist using the ABCD matrix formulism. We approximated the transverse temperature distribution difference $T(r)$ to be quadratic, using the following approximation for $T(r)$ given in [23],

$$\Delta T(r) = \Delta T(0)(1 - \alpha r^2), \tag{4.12}$$

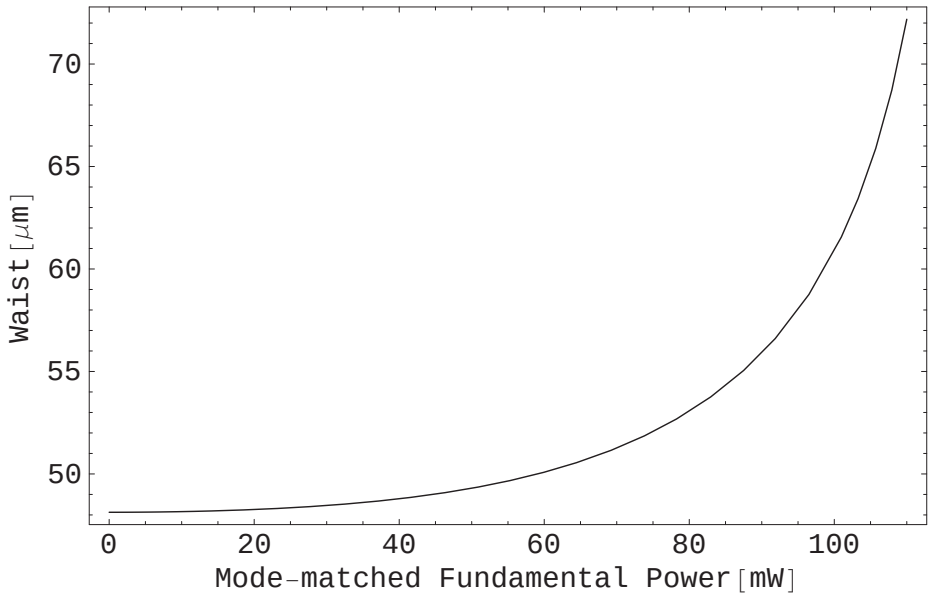

Figure 4.14 Optical resonator beam waist s_2 versus the mode-matched fundamental power.

$$\alpha = \frac{2}{a^2}[\ln \frac{2\gamma r^2}{a^2} - Ei(-\frac{2r^2}{a^2})]^{-1}, \tag{4.13}$$

with $\Delta T(0)$ is the axial temperature increase, Ei is the exponential integral given in [24], and $\gamma \equiv 1.781$. The above temperature distribution results in a corresponding variation in the transverse index of refraction given by

$$n(r) = n_o + \frac{\partial n_b}{\partial T} \triangle T(r), \tag{4.14}$$

where n_o is the index of refraction of potassium niobate, and $\frac{\partial n_b}{\partial T}$ is the thermal-optical coefficient for the transverse axis [25]. Thus, the crystal becomes a medium with a quadratic index profile [26], which produces a lens modification to the resultant ABCD matrix in Eq. 3.10.

We estimated $\Delta T(0)$ to be $\sim$2 degrees centigrade, by measuring the observed difference in oven temperature for optimum phase matching in locked and scan mode. Using this along with the value of $\frac{\partial n_b}{\partial T} = 3.3 * 10^{-5}/C^{\circ}$, we determined our quadratic index profile.

Figure 4.14 is a plot of the resonator beam waist incorporating the effect of thermal lensing into the resonator system. In this figure we illustrate the dependence of our resonator beam waist s_2 in the center of the crystal ($r = 0$) as function of input fundamental power. For input powers less than .075 W, changes to the resonator beam waist with input power are insignificant in the system. However, at higher input powers, the beam waist begins to increase dramatically in size. This increase beam waist size reduces ξ_{nL}, and therefore the amount of infrared power absorbed or harmonic power produced.

Comparison of Fig. 4.10 to Fig. 4.14 shows that deviations from the thin-dashed curve (no thermal lensing) and the thicker dashed curve (thermal lensing) of Fig. 4.10 occur at similar power levels to those in which the resonator beam waist significantly changes from its original size in Fig. 4.14.

Another thermal effect that occurs in our cavity is thermal locking [27]. Thermal locking occurs when the cavity resonance is dragged when sweeping the cavity from lower to higher frequencies (longer to shorter cavity spacing), as illustrated in the broader higher frequency cavity transmission peak in Fig. 4.15. This occurs since as the cavity passes through this mode the circulating power suddenly increases, which causes an increase in the crystal temperature. This temperature change, results in a change in index of refraction, thus cavity length. This thermal adjustment causes the cavity to remain on resonant with the laser light, and thereby locking the cavity to laser for a small time duration.

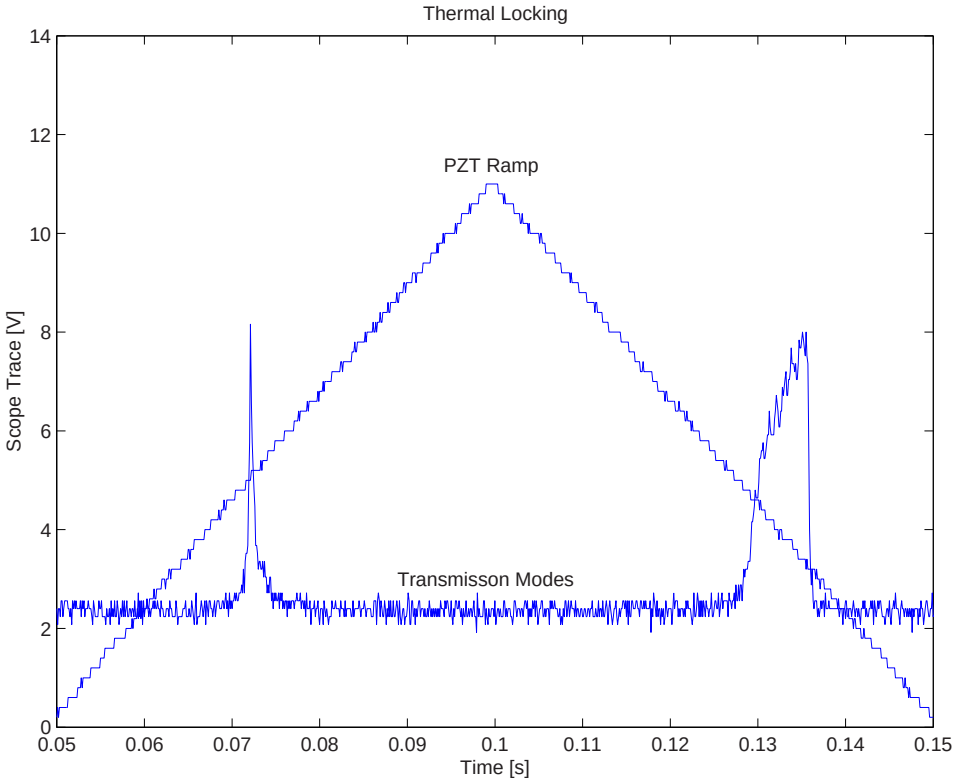

Figure 4.15 A oscilloscope trace illustrating thermal-self-locking. The apparent broadening of the line-shape to the right is a result of the resonance being dragged as the cavity is scanned.

Chapter 5
Feedback Electronics

An optical resonator is prone to external perturbations from the environment. For example, acoustical vibrations from nearby mechanical devices and thermal expansions and contractions due to temperature fluctuations can prevent our blue laser source from having a stable intensity output. However, by implementing feedback electronics we can achieve the desired state for our laser system.

Figure 5.1 is a diagram of the feedback network for our optical resonator. The network consists of four key elements: 1) The laser, including the input control of its frequency. This portion changes control voltage into laser frequency. 2) Cavity and RF electronics, which transform the laser frequency into an error signal. 3) Locking Electronics, the heart of which is an integrator, which changes volts of error signal into volts of control. 4) Summing junction, it is used for purposes of feedback into the laser system [32]. Overall, the loop diagram of Fig. 5.1 controls the laser frequency to lock the laser to the peak of the transmission mode, such that build-up is always maximal inside the cavity.

5.1 Error Signal

In our feedback control network, whether or not the laser is at a frequency that corresponds to maximal of transmission is indicated by the error signal. For our

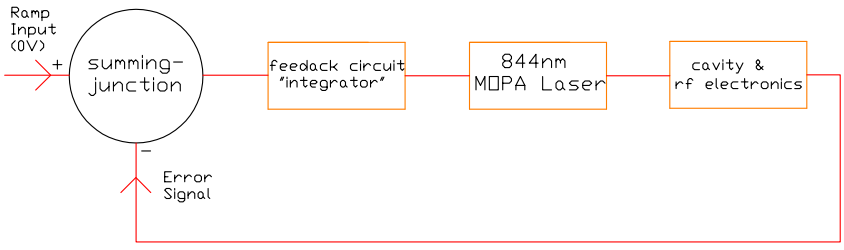

Figure 5.1 Diagram of feedback network.

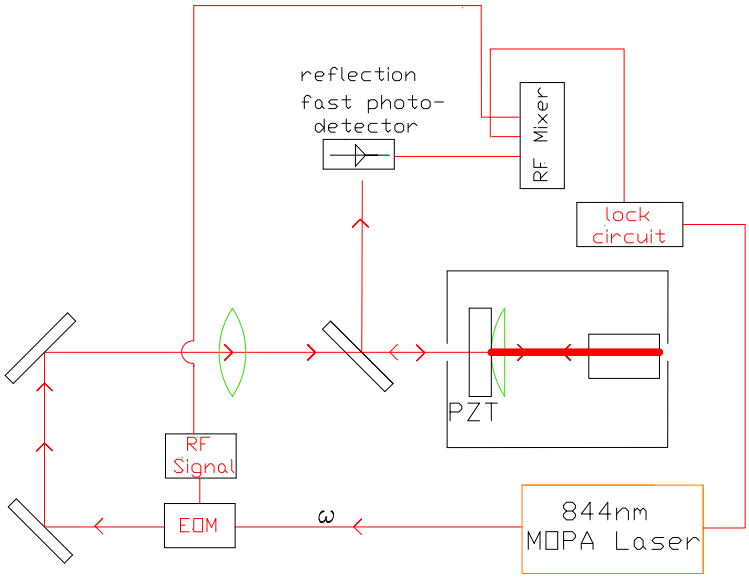

Figure 5.2 Optical and electronic set-up for the Pound-Drever locking experiment.

system, this is a voltage signal that is a function of laser frequency that contains essential information about the location of the modes inside the cavity. We produce this electronic signal to stabilize our system via the Pound-Drever-Hall method [28]. Our experimental set-up for this is illustrated in Figure 5.2.

The infrared light from the laser is frequency modulated at 17.8 MHz by a Electro-Optic-Modulator (EOM). This light is steered into the cavity where a fraction of it is reflected and transmitted. The reflected beam, after a series of optical elements, falls on a fast Thorlabs photo-diode. We then perform phase detection at 17.8 MHz using an electronic mixer to produce our error (demodulated) signal.

Figure 5.3 is a scope-trace of the error signal used to lock the 844 nm laser to the peak of the transmission mode. The signal can be derived using analysis given in [29]. It shape is essentially the derivative of the reflected mode lineshape. In addition, the error signal is antisymmetric, being negative on one side of the mode, positive on another, and zero at the cavity resonance. These features are important, because they indicate to the laser input controller, which direction to respond to compensate for

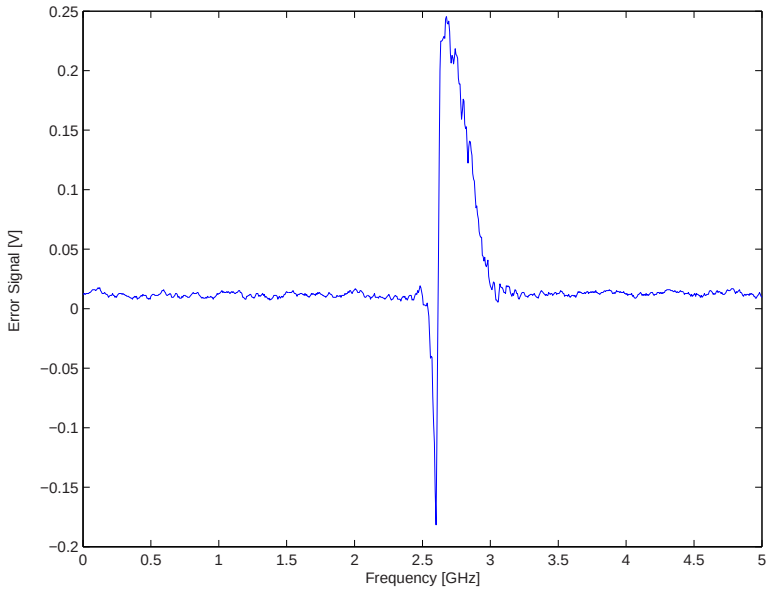

Figure 5.3 Error Signal for IR enhancement cavity produced by applying RF side-bands on 844 nm light. We scam the cavity in this illustration.

external perturbations. We use the error signal obtained as described above to lock the laser to the peak of our Fabry-Perot cavity transmission, to maintain maximal circulating and 422 nm power for each setting. The linear range about the zero, is called the locking slope (range), and gives a typical tuning range of .42 V per 41.7 MHz of the cavity mode.

5.2 Electronic Feedback

The electronic circuit in Fig. 5.4 is used to adjust and feedback the output voltage of the error signal to the laser such that its frequency corresponds to a transmission peak of the optical resonator. The heart of this circuit is an integrator, which has an output voltage, V_{out}, given by:

$$V_{out} = -\frac{1}{RC}\int V_{input}dt, \tag{5.1}$$

where R is the input resistor and C is the feedback capacitor.

If a perturbation shifts the cavity from resonance, a non zero voltage error signal

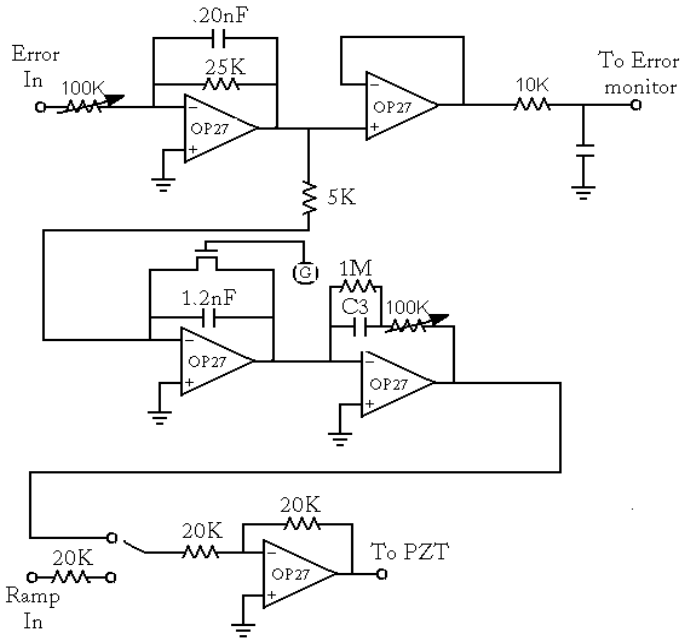

Figure 5.4 Diagram of the slow path servo-lock circuit used to lock the 844 nm laser to the cavity.

will be supplied to the integrator. For this input signal, the integrator's output signal rises steadily (integration over time). The rising output signal is amplified by the output stage of the servo-lock circuit in a Fig. 5.4 and is fed back into the commercial 844 nm laser driving PZT (input control), which sweeps the laser frequency back to the cavity resonance condition. As the laser frequency approaches the resonance condition, the error signal reaches zero volt. The integrator now maintains a zero volt output level, until another disturbance occurs.

5.3 Procedure to lock the laser

First, the initial settings are such that the servo loop in Fig. 5.4 is open, and only a ramp voltage from a function generator is applied to the Ramp In input, which is fed to the PZT to scan the optical resonator. Next, we reduce our scan to zero, and adjusts the PZT Offset (not shown) until we see resonance phenomena of our cavity. This centers the laser on the cavity resonance such that it falls within the circuit's lock range. Then we close the servo loop by switching the servo electronics from scan to lock mode and monitor the error signal (which is at zero volts). The servo loop will lock at the peak of the cavity transmission. Finally, we optimize the gain, G, of the output signal to the PZT control to get a tight lock.

5.4 Lock Improvements

We had to include an additional servo network, to achieve robust laser to cavity locking. The slow path feedback circuit, Fig. 5.4, controls the frequency of the laser using a PZT actuator that has a large frequency to voltage excursion ($\frac{MHz}{V}$), but slow response time. The slow response time of the PZT makes the servo loop of Fig. 5.4 inadequate for maintaining stable locking of our system, which is in the presence of acoustic vibrations with frequencies higher than the response frequency of the 844 nm laser's PZT. The servo loop illustrated in Fig. 5.5 has a much faster response time than the slow path servo loop of Fig. 5.5. The faster response time of this network is

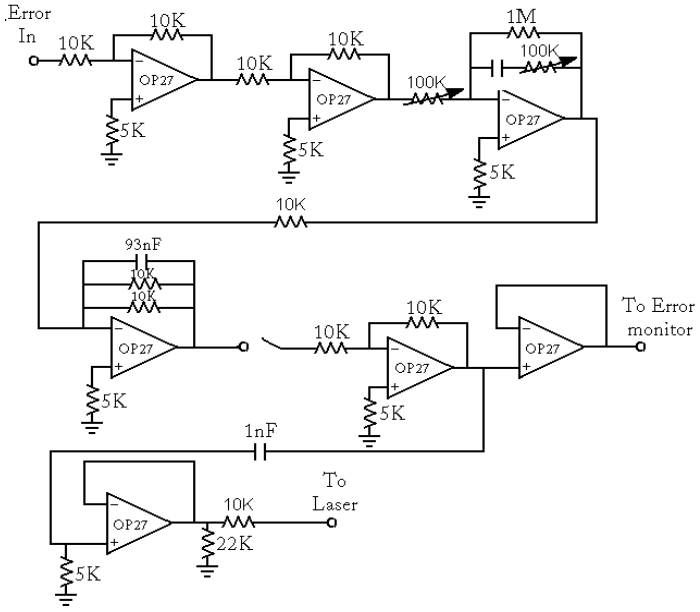

Figure 5.5 Diagram of the fast path current servo-lock circuit used to improve laser to cavity locking.

achieved by modulating the current of our 844 nm laser using the reflected power error signal, since the current source has a higher frequency response (16 kHz). This means the feedback response is very quick (response time is on time-scales proportional to the inverse of the servo-bandwidth). With this ability, we can compensate for external perturbations outside the bandwidth of our laser PZT response. As a result, we can maintain a stable lock for hours.

Chapter 6
Conclusions

6.1 Summary

We have illustrated the necessary steps for constructing a intensity stabilized blue laser source at 421.7 nm. We have explained the nonlinear optical concepts needed to make such a laser possible. Also, we described the use and purpose of an optical resonator in constructing such a laser. We typically run our blue laser with approximately 9 mW of light and we lock it to a strontium ion transition line for frequency stabilization. About 1 mW is used to optically image ultracold plasmas in our lab. This signifies the beginning of the use of a new and powerful technique to study ultracold plasmas [33].

6.2 Improvements

Figure 4.10 illustrates that the amount of harmonic power increase linearly with the fundamental power. Thus, as indicated by the figure, for higher input powers we should obtain more blue. Unfortunately, our system will be unable to behave in this manner, since our lock becomes unstable at these higher input powers. We believe this instability in our lock is a result of having a small cavity length.

For instance, for more power circulating in the cavity there is a corresponding increase in the crystals temperature. This increase in temperature causes a change in the crystal's optical path length. Since the crystal is about 20% of the cavity length, this effect alters the resonant frequency of cavity. In turn, the longitudinal mode of the cavity shifts, thereby causing our lock to come out of the locking range. However, if we can make the total cavity length much larger the length of the doubling crystal, our system will become more insensitive to changes in crystal length, therefore allowing us to achieve stability in our lock for higher input fundamental powers.

6.3 Future Experiments

The future use for this laser system is vast. We are currently using our blue laser source to image and measure the ion absorption spectrum. We are planing to use our laser to study ion acoustic waves, for determining the temperature of the electrons in the plasma. Further, the ultimate goal, is to use our blue laser source to laser cool and trap our ultracold neutral plasma. The ability to do this will allow us to access regimes in plasma physics not yet explored.

Appendix A
Circulating Power

The circulating power for our system can be determined by solving Eq. 3.1 by means of a series of successive or iterative approximations. The zero-order solution of Eq. 3.1 is given by:

$$P_c^0 = \frac{(1-R_a)P_{input}}{[1-\sqrt{R_aR_b(1-\ell-0)}]^2} \tag{A.1}$$

The first-order solution P_c^1 is obtained by inserting P_c^0 in the expression for C=$\xi_{nL}P_c$ in Eq. 3.1:

$$P_c^1 = \frac{(1-R_a)P_{input}}{[1-\sqrt{R_aR_b(1-\ell-\xi_{nL}[\frac{(1-R_a)P_{input}}{[1-\sqrt{R_aR_b(1-\ell-0)}]^2}])}]^2}. \tag{A.2}$$

The second order term is obtain by inserting Eq. A.2 into Eq. 3.1. Continuing in this manner, we obtained P_c to the forth order.

Figure A.1 is a plot of the circulating power as a function of input mode-matched fundamental power in the cavity. The solid curve is a plot of Eq. 3.1 with $C = 0$ (zero-order approximation). For 100 mW of mode-matched fundamental power input we obtain a peak circulating power of 4.4 W.

The thin-dashed curve in Fig. A.1 is a plot of Eq. 3.1 approximated to the forth-order. The value of ξ_{nL} is .004/W. For fundamental powers greater than 30 mW, infrared-to-blue conversion loss reduces the amount of power circulating in the cavity. The peak value of circulating power for this case is 3.2 W.

The thick-dashed curve in Fig. A.1 is a plot of Eq. 3.1 approximated to the forth-order including the effect of thermal lensing. The deviation between this curve and the thin-dashed curve occurs for input powers greater than 80 mW, and is a consequence of increase in the resonator beam waist size, s_2, inside the cavity. The increase in s_2 causes ξ_{nL} to reduce in magnitude, which in turn decreases the fraction of infrared power converted to blue. As a result, the amount of circulating power

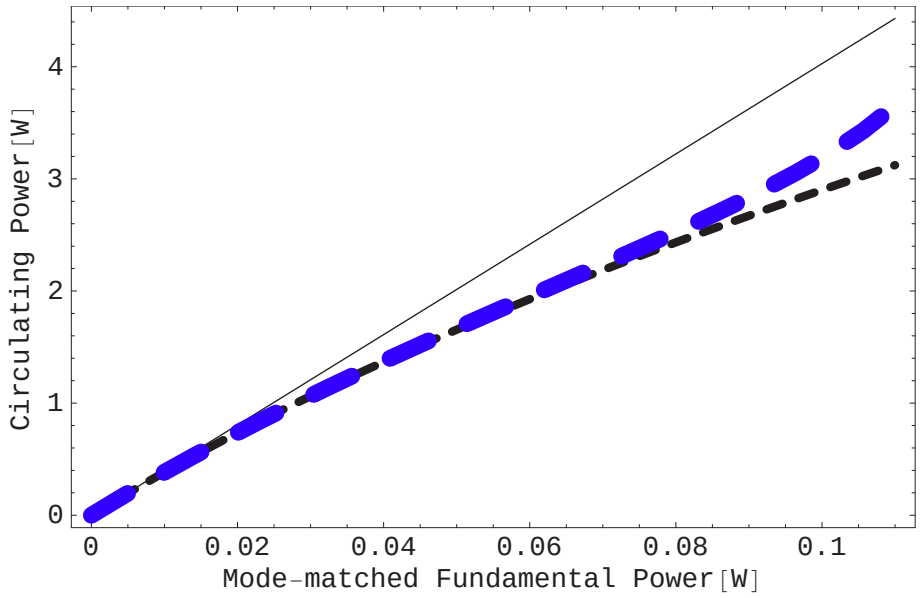

Figure A.1 The circulation power as a function of input mode-matched fundamental power in the cavity. The solid curve excludes infrared-to-blue conversion loss. The thin-dashed curve includes the effect of infrared-to-blue conversion loss on the build-up power in the cavity. The thick-dashed curve includes both the effects of infrared-to-blue conversion loss and thermal lensing on the circulating power.

increases in the cavity.

References

1. H. J. Metcalf and P. v. d Straten, *Laser Cooling and Trapping.* Springer, New York, first edition (1969).

2. S. Ichimaru, *Rev. Mod. Phys.* **54**, 1017 (1982).

3. P. Mansbach and J. Keck, *Phys. Rev.* **181**, 275 (1969).

4. M. S. Murillo, *Phys. Rev. Lett.* **87**, 115003 (2001).

5. T. C. Killian, S. Kulin, S. D. Bergerson, L. A. Orozco, C. Orzel, and S. L. Rolston. "Creation of an Ultracold Neutral Plasma", *Phys. Rev. Lett.* **83**, 4776 (1999).

6. S. Kulin, T. C. Killian, S. D. Bergerson, and S. L. Rolston. "Plasma Oscillations and Expansion of an Ultracold Neutral Plasma", *Phys. Rev. Lett.* **85**, 318 (1999).

7. K. J. Kuhn, *Laser Engineering.* Pretice-Hall, Inc., New Jersey, first edition (1975).

8. Ivan Biaggio, P. Kerkoc, L. S. Wu, and Peter Gunter. "Refractive indices of orthorhombic $KNbO_3$. II. Phase-matching configurations for nonlinear-optical interactions", *J. Opt. Soc. Am. B* **9**, 4 April (1992).

9. V. G. Dmitrev, G. G. Gurzadyan, and D. N. Nikogosyan. *Handbook of Nonlinear Optical Crystals*, Springer-Verlag, volume 64, Berlin, (1975).

10. Y. Uematsu, "Nonlinear Optical Properties of $KNbO_3$ single crystal in the orthorhombic phase", *Jpn. J. Appl. Phys.* **9**, (3) 380–386 (1992).

11. H. Kogelnik and T. Li, *Laser Beams and Resonators.* Proceedings of the IEEE, VOL. 54, NO. 10, OCTOBER (1966).

12. A. Maitland and M. H. Dunn, *Laser Physics.* John Wiley & Sons, Inc., New York, first edition (1969).

13. B. E. A. Saleh and M. C. Teich, *Fundamentals Of Photonics.* John Wiley & Sons, Inc., New York, (1991).

14. Anthony E. Siegman, *Lasers.* University Science Books, California, (1986).

15. Christoopher C. Davis, *Laers and Electro-Optics.* Cambridge University Press, New York, (1996)

16. M. Bode, I. Freitag, A. Tunnermann, and H. Welling. "Frequency-tunable 500-mW continous-wave all solid state single frequency source in the blue spectral Region", *Opt. Lett.* **22**, (16) 14 August (1997).

17. M. Lodahl, J. L. Sorenson, and E.S. Polzik. "High efficency second harmonic generation with a low power diode laser", *Appl. Phys. B* **64**, 383–386 (1997).

18. G. D. Boyd and D. A. Kleinman "Parametric interaction of focused guassian light beams", *J. Appl. Phys.* **39**, 3597 (1968).

19. H. Mabuchi, E. S. Polzik, and H. J. Kimble "Blue-light-induced infrared absorption in $KNBO_3$", *J. Opt. Soc. Am. B* **11**, 2023–2029 (1994).

20. L. E. Busse, L. Goldberg, and M. R. Surette, "Absorption losses in MgO-doped and undoped potassium niobate", *J. Appl. Phys.* **75**, 1102–1110 (1994).

21. Bruce G Klappauf. "Detailed Study of eficent blue laser source by second harmonic generation in a semi-monolithic cavity semi-monolithic cavity for cooling of strontium atoms", *Opt. Soc. Am.*, (2003).

22. A. D. Ludlow, H. M. Nelson, and S.D. Bergson. "Two-photon absorption in potassium niobate", electronic pre-prints.

23. E .S. Polzik and H.J. Kimble, "Frequency doubling with $KNbO_3$ in an external cavity", *Opt. Lett* **16**, (18) 15 Setember (1991).

24. M. Abramowitz and I. A. Stegun, *Handbook of Mathematical Functions.* Dover, New York, (1970), p. 228.

25. Gorachand Ghosh. "Dispersion of thermo-optic coefficients in a potassium niobate nonlinear crystal", *Appl. Phys. Lett.* **65**, (26) 26 December (1994).

26. A. Yariv. *Quantum Electronics.* John Wiley & Sons, Inc., New York, second edition (1975).

27. P. Dube, L. -S. Ma, J. Ye, P. Junger, and J. L. Hall. "Thermally induced self-locking of an optical cavity by overtone absorption in acetylene gas", *J. Opt. Soc. Am. B* **13**, (9) 9 September (1996).

28. P. W. P. Drever et al. "Laser Phase and Frequency Stabilization Using an Optical Resonator", *Appl. Phys. B* **31**, 97–105 (1983).

29. G. C. Bjorklund et al. "Frequency-modulation (FM) Spectroscopy-Theory of Line Shapes and Signal-to-noise Analysis", *Appl. Phys. B* **31**, 145 (1983).

30. M. L. Boas, *Mathematical Methods In The Physical Sciences.* John Wiley & Sons, New York, second edition (1970), p. 509.

31. J. M. W Kruger. *A Novel Technique For Frequency Stabilizing Laser Diodes.* M.S., University of Otago (1998).

32. Paul Horowitz and Winfield Hill, *The Art of Electronics.* Cambridge University Press, New York, second edition (1989).

33. C. E. Simien, Y. C. Chen, P. Gupta, S. Laha, Y. N. Martinez, P. G. Mickelson, S. B. Nagel, and T. C. Killian. "Using Absorption Imaging to Study Ion Dynamics in an Ultracold Neutral Plasma", *Phys. Rev. Lett.* **92**, 143001 (2004).